Numerical study of nitrogen oxides chemistry during plasma assisted combustion in a sequential combustor

Quentin Malé[a,*], Nicolas Barléon[b], Sergey Shcherbanev[a], Bayu Dharmaputra[a], Nicolas Noiray[a,*]

[a]*CAPS Laboratory, Department of Mechanical and Process Engineering, ETH Zürich, 8092 Zürich, Switzerland,*
[b]*CERFACS, 42 avenue Gaspard Coriolis, 31057 Toulouse, France,*

Abstract

Plasma Assisted Combustion (PAC) is a promising technology to enhance the combustion of lean mixtures prone to instabilities and flame blow-off. Although many PAC experiments demonstrated combustion enhancement, several studies report an increase in NO_x emissions. The aim of this study is to determine the kinetic pathways leading to NO_x formation in the second stage of a sequential combustor assisted by Nanosecond Repetitively Pulsed Discharges (NRPDs). For this purpose, Large Eddy Simulation (LES) associated with an accurate description of the combustion/NO_x chemistry and a phenomenological model of the plasma kinetics is used. Detailed kinetics 0-Dimensional reactors complement the study. First, the LES setup is validated by comparison with experiments. Then, the NO_x chemistry is analyzed. For the conditions of operation studied, it is shown that the production of atomic nitrogen in the plasma by direct electron impact on nitrogen molecules increases the formation of NO. Then, the NO molecules are transported through the turbulent flame without being strongly affected. This study illustrates the need to limit the diatomic nitrogen dissociation process in order to mitigate harmful emissions. More generally, the very good agreement with experimental measurements demonstrates the capability of LES combined with accurate models to predict the NRPD effects on both turbulent combustion and NO_x emissions.

---

*Corresponding authors

  Email addresses: `qumale@ethz.ch` (Quentin Malé), `noirayn@ethz.ch` (Nicolas Noiray)

Novelty and Significance Statement

In this work, a novel high-fidelity Large Eddy Simulation (LES) setup is used for the first time to study the effects of Nanosecond Repetitively Pulsed Discharges (NRPDs) on the formation of NO_x. The LES setup includes an accurate description of the combustion and NO_x chemistry with an innovative sophisticated modeling of the plasma discharges to account for the impact on the NO_x formation. Massively parallel computations of a lab-scale sequential combustor are performed and results are compared with experimental data. Chemical pathways for the formation of NO_x due to NRPDs are studied for the first time in a real burner. This is of major importance to limit the NO_x emissions that can occur under certain conditions during plasma assisted combustion. The excellent agreement with the experimental data demonstrates the capability of the original LES setup to retrieve the NRPD effects on the turbulent flame and on the formation of NO.

Author Contributions

Q.M. and N.N. conceived the research idea. Q.M. led the numerical simulation investigations. S.S. and B.D. performed the experiments. N.B. and Q.M. set up the plasma modeling framework. All authors discussed the results. The manuscript was written by Q.M. All authors reviewed and approved the final version of the manuscript.

1. Introduction

Plasma Assisted Combustion (PAC) is being actively developed to improve combustion systems efficiency and to reduce harmful emissions. In particular, PAC can help to control ultra lean combustion, to develop low NO_x emissions hydrogen combustion technologies, or to control the combustion of alternative fuels [1]. Nanosecond Repetitively Pulsed Discharges (NRPDs) have been successfully applied to enhance the combustion in various combustion systems. A recent state of the art has been presented in Ref. [2]. For example, NRPDs have been shown to significantly extend lean combustion limits (e.g., [3, 4, 5, 6, 7, 8, 9]), suppress unstable combustion regimes (e.g.,

[10, 11]) and improve flame anchoring (e.g., [12, 13]), in combustors relevant for gas turbine applications.

Although the results to date are very promising, some studies report an increase in NO_x emissions when plasma discharges are used [14, 15, 16, 5], without investigating in detail the origin of these emissions. This could be due to the interaction of the plasma with the N_2 molecules. The plasma can, for example, dissociate N_2 by direct electron impact

$$e^- + N_2 \longrightarrow e^- + N + N. \tag{R1}$$

The N atom can then be responsible for NO production through the reactions

$$N + O_2 \rightleftharpoons NO + O, \tag{R2}$$

$$N + OH \rightleftharpoons NO + H \text{ and} \tag{R3}$$

$$N + O + M \rightleftharpoons NO + M. \tag{R4}$$
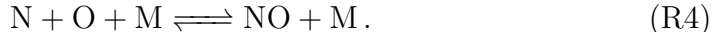
Other species can also act on the NO_x formation. For example, atomic oxygen is known to be generated by the dissociative quenching of electronically excited diatomic nitrogen $N_2{}^*$ with O_2 [17]

$$N_2{}^* + O_2 \rightleftharpoons 2O + N_2, \tag{R5}$$
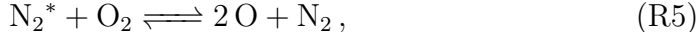
and it can then react with N_2 to form NO through

$$N_2 + O \rightleftharpoons NO + N. \tag{R6}$$

The atomic N from Eq. (R6) can then trigger Eq. (R4). Furthermore, plasma discharges in H_2O-containing mixtures can generate OH molecules that will set off Eq. (R3). Plasma discharges are therefore a potential source of NO_x. However, it is also known that the flame following the plasma can consume nitrogen oxides, similar to a reburn process [14]. The study of the NO_x chemical kinetics during PAC is therefore extremely complex because of the coupling between the plasma, combustion, and NO_x chemistry.

In this work, Large Eddy Simulation (LES)—supported by experiments—is used as a tool to investigate the formation of nitrogen oxides in the second stage of a sequential combustor assisted by NRPDs where:

- The sequential burner is fed with a mixture containing combustion products from the first stage flame, including NO_x.

- The burnt gas produced by the first stage undergoes intense cooling and turbulent mixing with cold dilution air and secondary fuel injection.

- The mixture of vitiated air and fuel is stratified in the sequential burner, both in terms of composition and temperature.

- The plasma induces an excitation of the species flowing between the electrode system, resulting in rapid heating, slow heating, and the generation of active species in the reactive flowing mixture.

- The turbulent combustion process that occurs in the second stage is affected by the plasma generated upstream.

The objective of this study is to clarify the mechanisms responsible for the formation of NO_x in this highly complex environment. Only a massively parallel LES of the full sequential stage can address this properly. From a numerical point of view, this involves multiple challenges:

- The multitude of physical processes considered (i.e., turbulent mixing, turbulent combustion, NO_x chemistry, plasma chemistry, combustion chemistry) requires a powerful and scalable multi-physics computation code.

- The interaction of NO_x, plasma and combustion chemistry demands a sophisticated description of the chemical kinetics.

- The computational cost associated with the spatial and temporal resolution of the plasma discharges including the description of the electric field in a 3-Dimensional (3D) high Reynolds flow is prohibitive. A model capturing all important plasma effects must be derived to enable 3D turbulent reactive flow simulation in realistic geometries.

- Even simplified, plasma effects occur on a very small time scale both in time and space compared to combustion processes. The integration of the plasma requires very small grid cells ($\Delta_x \approx 100$ μm) and very small time steps ($\Delta_t \approx 0.1$ ns) which increases the computational cost considerably.

4

- In addition to a plasma model and a reasonably complete description of chemistry, a proper method to model subgrid scale turbulence-chemistry interaction is also needed for the turbulent flame of the second stage combustion chamber.

This paper shows how sophisticated/high performance simulation tools combined with experiments can be used to advance recent combustion technology by gaining knowledge about the physical phenomena involved. First, the configuration of the sequential combustor and the operating points chosen for this work are described. Then, the simulation and modeling methods set up are detailed. Finally, the results of the simulations are analyzed to study the NO_x formation mechanisms. The LES data are supported by experimental measurements.

2. Sequential combustor configuration

This numerical study is based on experimental tests performed with a laboratory scale sequential combustor operated at atmospheric pressure. The first stage consists of an array of 4×4 technically premixed jet flames, which generate hot combustion products. The focus of this work is on the sequential stage where NRPDs are applied. Therefore, only this stage is simulated. Figure 1 shows a diagram of the sequential stage together with the simulation and modeling tools implemented for the study. The sequential stage features a dilution air mixer with large lateral vortex generators and multiple air injection holes for rapid mixing, a Sequential Burner (SB) in which fuel is injected axially and mixes with the co-flow of hot vitiated air, a pin-to-pin electrodes arrangement in the SB which enables NRPD generation upstream of the burner outlet, and the sequential combustion chamber. The inlet composition and temperature are defined by the combustion products of the first stage: a 1-Dimensional (1D) laminar flame is used to estimate the combustion products of the first stage flame, then, the mixture evolves in a 0-Dimensional (0D) reactor for a time equal to the residence time until the inlet of the sequential stage dilution air mixer. The validity of this approach is assessed by comparing the NO concentration level without second stage fuel injection between the experiment and the simulation ("2nd stage off" in Fig. 11).

Throughout this study, the thermochemical state of the vitiated air flow that feeds the sequential stage is fixed. The first stage flue gas results from
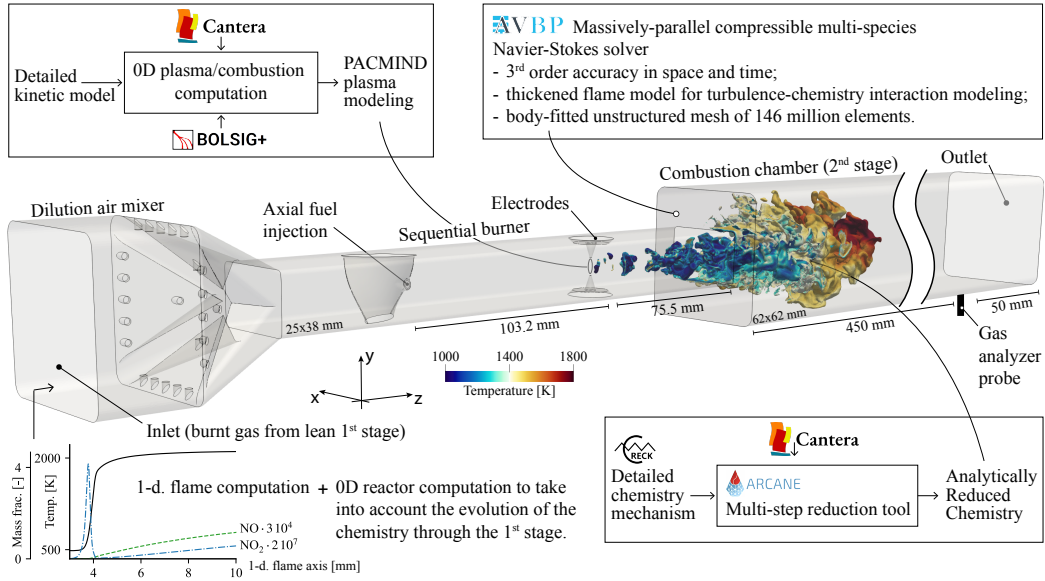
Figure 1: Diagram of the sequential stage with the detail of its geometry and its components, as well as the illustration of the numerical tools used to perform the LESs including the plasma effects and the NO_x chemistry. The temperature colored isosurface of heat release rate depicts the flame assisted by plasma in the sequential stage.

the combustion of 15 g/s of air with 0.7 g/s of methane at 503.15 K, the equivalence ratio is 0.8. It is then diluted with 18 g/s of air at ambient temperature. A CH_4/H_2 fuel blend is used in the sequential stage. The mass flows of methane and hydrogen are 0.6 g/s and 0.07 g/s, respectively. The global equivalence ratio in the sequential stage is 0.6, the flame thermal power is 38.4 kW.

High voltage pulses are applied at a certain Pulse Repetition Frequency (PRF) to locally generate multiple NRPDs between the electrodes. All operating points are summarized in Table 1, including details on plasma discharges where applicable. E^p is the pulse deposited energy measured experimentally. P^p is the mean plasma power defined as

$$P^p = E^p \, \mathrm{PRF} \,. \tag{1}$$

In the experiments, the reacting flow in the 2nd stage of the sequential combustor is characterized by recording OH^* chemiluminescence. The detection system consists of a high-speed CMOS camera (LaVison Star X) coupled to a high-speed intensifier (LaVision HS-IRO), equipped with a CERCO UV

6

Label	Fuel inj.	Voltage	E^p	PRF	P^p
2nd stage off	no	-	-	-	-
NRPD off	yes	-	-	-	-
14 kV, 20 kHz	yes	14 kV	1.21 mJ	20 kHz	24.2 W
14 kV, 40 kHz	yes	14 kV	2.07 mJ	40 kHz	82.8 W

Table 1: Varied parameters for the different Operating Points (OPs) studied in the sequential stage. The labels will be used later to refer to the different OPs.

lens (45 mm, F/1.8) and a bandpass filter (Edmund Optics, centered at 310 nm, FWHM 10 nm). The camera frame rate is set to 5 kHz with an intensifier gate width of 40 μs. The emission from the discharges is much more intense than the OH* emission of the flame. An optical obstacle is therefore used to mask the discharge location and to prevent damage to the IRO-intensifier.

Characterization of the discharge geometry was performed during a previous experimental campaign [9]. The volume of the discharge is estimated as a cylinder with a radius of 500 μm and a length of 5 mm. These measurements were obtained from an average of 100 image samples of the plasma channel. The images were acquired with a camera equipped with a narrow band 337$\pm$5 nm filter, capturing the most intense band of N_2(C-B)(0-0) transition.

The exhaust gas analysis is performed using an ABB EL3040 gas analyzer (sampling rate 1 Hz) with an Uras26 infrared photometer. The device has a 7.9% relative extended uncertainty on NO measurements in the range 0-200 mg/Nm^3. The sampling is performed for 30 s of operation near the outlet of the sequential combustor, 450 mm after the inlet of the 2nd stage combustion chamber (Fig. 1), through a 2 mm pinhole of a gas probe. The dry NO emissions are reported in terms of mg/Nm^3, conditioned at 276.15 K.

3. Numerical model and methods

3.1. Plasma modeling

During each high-voltage nanosecond pulse, the kinetic energy of the electrons increases. Subsequently, this energy is transferred to the surrounding heavy particles through collisional processes, giving rise to excited particles, ions and radicals. Despite the recent efforts to reduce Non Equilibrium Plasma (NEP) chemical kinetics [18, 19, 20], the computational cost of solving the electric field, the electron energy, the continuity equations for charged

7

and excited species, in addition to the Navier-Stokes equations for reactive flows is very high. The integration of NEP effects in 3D simulations of turbulent reactive flows inside complex geometries can only be achieved with simplified models that incorporate all relevant plasma effects for the considered study. Such a model has been developed by Castela et al. [21], incorporating the most important effects of NEP in a N_2/O_2 mixture. In this model, the relaxation of electronically excited N_2 molecules translates into a fast increase of the gas temperature and into the fast dissociation of O_2 molecules, whereas the relaxation of vibrationally excited N_2 molecules translates into a slower heat release. The model has been successfully applied to analyze the flow induced by a plasma discharge in a Direct Numerical Simulation (DNS) framework [22]. It has also been successfully applied in a LES framework to study turbulent flame ignition [23], turbulent combustion enhancement [24] and stabilization [9]. Although this simple model has proven to be very effective, it does not account for secondary effects that may be responsible for the production of NO_x. A more complex model must therefore be used for the present study. Recently, Barléon et al. [25] have extended the phenomenological approach of Castela et al. [21] to take into account more plasma processes involved in methane-air mixtures, including the production of N and NO, which is crucial for the study of NO_x formation. Therefore, this approach will be used in this work. As in Ref. [21], the discharge power $\dot{E}^p$ is divided into three contributions:

$$\dot{E}^p = \dot{E}^p_{\text{chem}} + \dot{E}^p_{\text{heat}} + \dot{E}^p_{\text{vib}} \,, \tag{2}$$

where $\dot{E}^p_{\text{chem}}$, $\dot{E}^p_{\text{heat}}$ and $\dot{E}^p_{\text{vib}}$ are the amount of power that goes into chemical effects, fast gas heating and vibrational excitation, respectively. However, $\dot{E}^p_{\text{chem}}$ is here divided into several global processes instead of a single one in the original work of Castela et al. [21]. This allows to consider a wide variety of chemical processes occurring during the discharge. The amount of power that goes into chemical effects reads

$$\dot{E}^p_{\text{chem}} = \sum_{j=1}^{P} \alpha_j \dot{E}^p = \alpha_{\text{chem}} \dot{E}^p \,, \tag{3}$$

where α_j is the fraction of the discharge power which contributes to the process j and $\alpha_{\text{chem}} = \sum_{j=1}^{P} \alpha_j$ is the global chemical energy fraction resulting from P processes. The amount of power that goes into fast gas heating and

vibrational excitation read

$$\dot{E}^p_{\text{heat}} = \alpha_{\text{heat}}\dot{E}^p \text{ and } \dot{E}^p_{\text{vib}} = \alpha_{\text{vib}}\dot{E}^p \,, \tag{4}$$

respectively. The discharge energy fraction coefficients α characterize the discharge effects. These coefficients satisfy:

$$\sum_{j=1}^{P} \alpha_j + \alpha_{\text{heat}} + \alpha_{\text{vib}} = 1 \,. \tag{5}$$

The difficulty now lies in determining the α coefficients and the important P processes, that depend on the gas thermochemical state $\mathcal{S} = (Y_{k=1,\ldots,N_s}, T, P)$ and the electric field E, where N_s is the number of species in the gas mixture. A precise methodology has been established by Barléon et al. [25] for this purpose. First, detailed kinetic simulations are conducted using isochoric plasma reactors following the approach described in Ref. [20]. These simulations include detailed plasma-combustion kinetics, which consider electron impact reactions, ion chemistry, vibrational and electronic excitation and relaxation. Second, an analysis of the species production rate from plasma processes issuing from the detailed plasma kinetics $\dot{\omega}^{p,*}_k$ determines how the discharge energy is split into chemical, fast heating, and vibrational effects. The α coefficients are ultimately computed to integrate the NEP effects into the LES equations (Section 3.3) where only ground state neutral species are considered. A precise description of the method for determining the α coefficients is given in Ref. [25]. It is not reported here for brevity reasons. Table 2 gives the global processes used to model the NEP discharge effects for the present study, for which NO_x production must be taken into account and NRPDs are applied in a mixture of vitiated air and fuel. For now, the plasma model neglects the presence of hydrogen molecules in the gas mixture. It is verified in Section 4.1 that this simplification does not significantly affect the outcome by comparing the modeling results with a detailed plasma-combustion chemistry.

3.2. Analytically reduced chemistry

The study of NO_x chemistry in a sequential combustor with plasma discharges requires a precise description of the chemical kinetics able to account for the evolution of pollutants as well as ignition induced by the

	Dominant physical processes	Global process
1	$e^- + O_2 \longrightarrow e^- + 2O$ $N_2\,(\,A_3,\ B_3, C_3, a_1) + O_2 \longrightarrow N_2 + 2O$	$O_2 \longrightarrow 2O$
2	$e^- + N_2 \longrightarrow e^- + N + N\,(^2D)$	$N_2 \longrightarrow 2\,N$
3	$N\,(^2D) + O_2 \longrightarrow NO + O$	$O_2 + N_2 \longrightarrow 2NO$
4	$e^- + CH_4 \longrightarrow e^- + CH_3 + H$ $N_2\,(\,A_3,\ B_3, C_3, a_1) + CH_4 \longrightarrow N_2 + CH_3 + H$	$CH_4 \longrightarrow CH_3 + H$
5	$e^- + CO_2 \longrightarrow e^- + CO + O$ $N_2\,(\,A_3,\ B_3, C_3, a_1) + CO_2 \longrightarrow N_2 + CO + O$	$CO_2 \longrightarrow CO + O$
6	$e^- + H_2O \longrightarrow e^- + OH + H$ $N_2\,(\,A_3,\ B_3, C_3, a_1) + H_2O \longrightarrow N_2 + OH + H$	$H_2O \longrightarrow OH + H$
7	$CH_4 + O\,(^1D) \longrightarrow CH_3 + OH$	$CH_4 + \frac{1}{2}O_2 \longrightarrow CH_3 + OH$

Table 2: Description of the global processes considered in this work to model the NEP discharge effects.

NRPDs, auto-ignition, flame consumption rate and stretch response. Analytically Reduced Chemistry (ARC) mechanisms—whose application to reacting flows is widely described by Felden [26]—allow to accurately describe these phenomena, while keeping the computational cost at an affordable level [27, 28, 29, 9, 30].

The ARC mechanism is specially constructed for this work using the ARCANE library [31], co-developed by CERFACS and Cornell University. ARCANE includes a multi-step reduction tool relying on Directed Relation Graph with Error Propagation (DRGEP) [32], chemical lumping [33] and Quasi-Steady State (QSS) approximation [34]. Reduction starts from the CRECK mechanism [35, 36] with an appropriate NO_x sub-mechanism from Ref. [37]. The detailed mechanism comprises 159 species and 2459 reactions. A set of canonical 1D or 0D configurations is used to steer the reduction process towards an accurate ARC mechanism. The configurations include 1D premixed laminar flames and 0D homogeneous reactors. The fresh gas conditions of the set of 1D flames are representative of the conditions encountered in the sequential stage, with variations of the mixture fraction Z around the perfectly mixed mixture fraction $Z^{PM} = 0.0195$. The mixture fraction is defined here between the fuel ($Z = 1$) and the vitiated air after the dilution air mixer ($Z = 0$). The initial conditions of the set of 0D reactors are similar. Nevertheless, additional 0D reactor configurations are needed to keep the core of the physics of the plasma-induced ignition and

NO$_x$ chemistry. Cases where the initial mixture is doped by an addition of atomic oxygen are created to mimic plasma ignition [38, 9]. Cases where the initial mixture is doped by an addition of NO and NO$_2$ are created to mimic the effects of NO$_x$ on the acceleration of CH$_4$ oxidation [37]. The final ARC mechanism contains 39 species (18 of them in quasi-steady state) and 198 reactions (see Supplemental Material).

Figure 2 shows the laminar flame speed and the auto-ignition time predicted by the reference chemistry and the ARC chemistry for a wide range of mixture fractions, computed with Cantera [39]. A good agreement is observed between the detailed and the new ARC mechanism. The evolution of the NO$_x$ through the flame is also consistent (Fig. 3). In order to assess the capability of the ARC scheme to capture the plasma effects, a low energy NEP discharge $E^p = 0.25$ mJ is applied in a 0D reactor with a reduced electric field $E/N = 250$ Td representative of the current work (Fig. 4). The volume of the discharge is experimentally estimated as a cylinder with a radius of 500 μm and a length of 5 mm (Section 2). This results in an energy density $e^p = 0.064$ J/cm^3. The ignition time and the species evolution are correctly retrieved. The enhancement of CH$_4$ oxidation by NO and NO$_2$ molecules is assessed using Perfectly Stirred Reactors (PSR) at specific conditions for which the mechanism has been validated [37]. The PSR computations are performed at 107 kPa, filled with a mole fraction ratio CH$_4$/O$_2$/NO = 0.01/0.01/0.0005 and CH$_4$/O$_2$/NO$_2$ = 0.01/0.01/0.0004, both balanced with Argon (Fig. 5). This corresponds to the experimental conditions of Ref. [37], whose pressure is close to the atmospheric pressure of our burner. The acceleration of the CH$_4$ oxidation is accurately reproduced. These validation cases demonstrate that the chemical pathways of interest for the present work were correctly kept during the reduction process. The behavior of the reduced kinetic system is suitable for the accurate description of plasma assisted combustion and NO$_x$ chemistry under the conditions of the sequential combustor studied.

3.3. Large eddy simulation

The LESs are computed using the AVBP code [40, 41]. AVBP is an unstructured cell-vertex massively-parallel code solving the compressible multi-species Navier-Stokes equations. The discretization of the convective terms is done using the fully explicit Two-step Taylor–Galerkin C (TTGC) finite element numerical scheme [42]. TTGC offers third order accuracy in space and time on irregular grids. The effects of the unresolved small-scale fluid
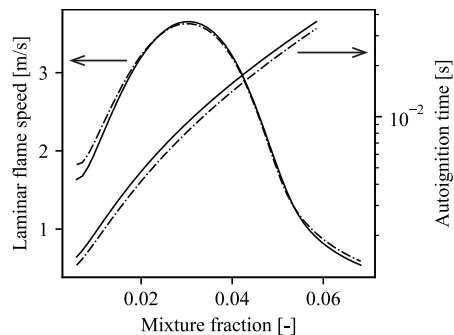
Figure 2: Laminar flame speed and auto-ignition time predicted by the reference chemistry (——) and the ARC chemistry (-··-·). The mixture fraction is defined from the composition of the vitiated air and the fuel.
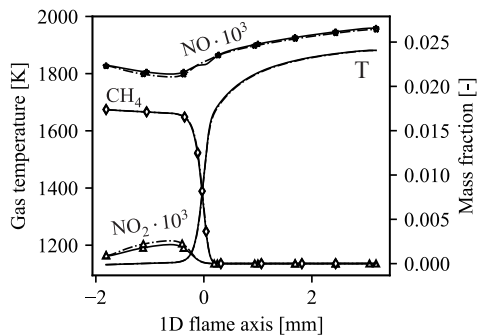

Figure 3: Profiles of temperature and species mass fraction predicted by the reference chemistry (——) and the ARC chemistry (-··-·) for a 1D laminar flame at perfectly mixed conditions, equivalence ratio $\phi = 0.6$.

motions are modeled using the SIGMA [43] subgrid-scale model. The so-called Thickened Flame (TF) model [44] is used to resolve the reactive zone of the flames computing the reaction rates issuing from the ARC mechanism directly on the grid. Its dynamic formulation is used here [45]: the correction of the TF model is applied only where a reactive zone is detected by a flame sensor modeled as a function of the fuel consumption rate [27]. The thickening factor is adapted to the local size of the cells in the mesh. Unresolved flame wrinkling effects are accounted for using an efficiency function based on the wrinkling factor of Charlette et al. [46]. Flame thickening is not triggered in the discharge region so that it does not influence the ignition induced by the NRPDs. To ensure a correct resolution of the physical phenomena related to the NRPDs, a very fine mesh is used between the discharge zone and the
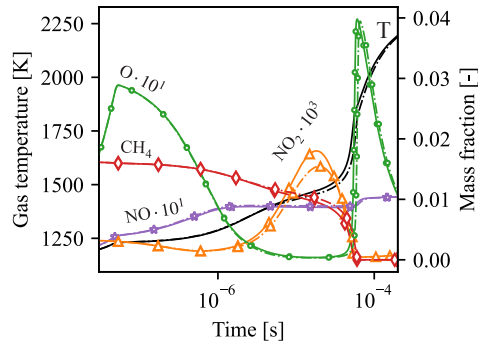
Figure 4: Gas temperature and species mass fraction after a NEP discharge modeled using the approach described in Section 3.1 for the reference chemistry (——) and the ARC chemistry (-··-). $E/N = 250$ Td, $e^p = 0.064$ J/cm^3, the initial thermochemical state corresponds to perfectly mixed conditions.
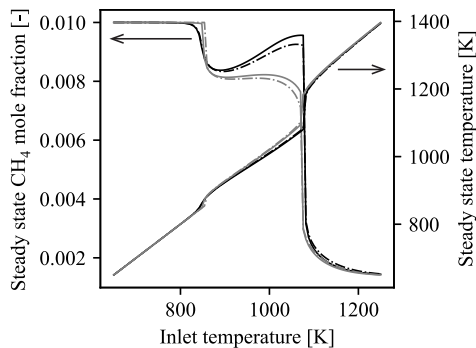

Figure 5: Steady-state methane mole fraction and gas temperature in a PSR as defined in Ref. [37], function of the inlet temperature for the reference chemistry (——) and the ARC chemistry (-··-). Black lines: $X_{NO} = 500$ ppm. Gray lines: $X_{NO_2} = 400$ ppm. 107 kPa, equivalence ratio $\phi = 2$, diluted with Argon.

outlet of the Sequential Burner (SB). This approach has already proven to be able to account for plasma physics in the same combustor [9]. Schulz et al. have also validated the modeling approach in a similar sequential combustor [47].

The effects of the plasma described by the phenomenological model detailed in Section 3.1 are integrated into the LES balance equations. Since plasma chemistry is much faster than flow mixing, its subgrid-scale interaction with turbulence is neglected [23]. The filtered species mass balance

13

equations read

$$\frac{\partial \bar{\rho}\widetilde{Y_k}}{\partial t} + \frac{\partial}{\partial x_j}\left(\bar{\rho}\widetilde{Y_k}\widetilde{u_j}\right) = -\frac{\partial}{\partial x_j}\left[\overline{J_{j,k}} + \overline{J_{j,k}}^t\right] + \frac{\mathcal{E}}{\mathcal{F}}\dot{\omega}_k^c + \dot{\omega}_k^p \text{ for } k = 1, N_s\,, \quad (6)$$

where $\bar{\varphi}$ and $\widetilde{\varphi}$ are the Reynolds and Favre filtering of a variable φ. ρ is the gas density, Y_k the mass fraction of the species k, and u_j the velocity along the direction j. $\overline{J_{j,k}}$ is the filtered diffusive flux and $\overline{J_{j,k}}^t$ the subgrid-scale flux of the species k. $\mathcal{E}$ and $\mathcal{F}$ are the efficiency and the thickening factor of the TF model, respectively. $\dot{\omega}_k^c$ and $\dot{\omega}_k^p$ are the source term of the species k due to combustion and plasma kinetics, respectively. The balance equation for the total non-chemical energy E, sum of the sensible and kinetic energy, reads

$$\frac{\partial \bar{\rho}\widetilde{E}}{\partial t} + \frac{\partial}{\partial x_j}\left(\bar{\rho}\widetilde{E}\widetilde{u_j}\right) = -\frac{\partial}{\partial x_j}\left[u_i\left(P\delta_{ij} - \tau_{ij}\right) + \overline{q_j} + \overline{q_j}^t\right] + \frac{\mathcal{E}}{\mathcal{F}}\dot{\omega}_T + \dot{E}_{\text{heat}}^p + \dot{R}_{\text{VT}}^p\,, \tag{7}$$

where P is the pressure and δ_{ij} the Kronecker symbol. τ_{ij} is the viscous tensor. $\overline{q_j}$ is the filtered energy flux and $\overline{q_j}^t$ the subgrid-scale energy flux in the direction j. $\dot{\omega}_T$ is the Heat Release Rate (HRR) due to combustion. The filtered momentum balance equations are unchanged. In addition, a balance equation is solved for the out-of-equilibrium vibrational energy e_{vib}:

$$\frac{\partial \bar{\rho}\widetilde{e_{\text{vib}}}}{\partial t} + \frac{\partial}{\partial x_j}\left(\bar{\rho}\widetilde{e_{\text{vib}}}\widetilde{u_j}\right) = \left(\left[\frac{\bar{\mu}}{S_{c,e_{\text{vib}}}} + \frac{\mu_t}{S_{c,e_{\text{vib}}}^t}\right]\frac{\partial \widetilde{e_{\text{vib}}}}{\partial x_i}\right) + \dot{E}_{\text{vib}}^p - \dot{R}_{\text{VT}}^p\,, \tag{8}$$

where a classical Fick's law is used for the molecular and turbulent diffusion. μ is the dynamic viscosity and S_c the Schmidt number. It is assumed that e_{vib} diffuses as N_2 (i.e., $S_{c,e_{\text{vib}}} = S_{c,N_2}$) which are the dominant vibrationally excited molecules. The relaxation term $\dot{R}_{\text{VT}}^p$ that appears in Eqs (7) and (8) controls the rate at which the out-of-equilibrium vibrational energy is converted to translational energy (i.e., gas heating). This relaxation is dominated by

$$N_2\,(v{=}1) + M \longrightarrow N_2\,(v{=}0) + M + \text{heat}\,, \tag{R7}$$
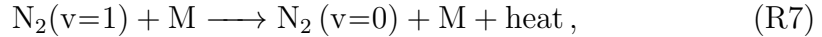
that slowly heats the gas. The rate of Eq. (R7) strongly depends on the colliding partner M for which N_2, O_2, CO_2, H_2O, H_2, OH, H and O are

considered. The relaxation term $\dot{R}^p_{\mathrm{VT}}$ is computed using the Landau-Teller harmonic oscillator assumption [48, 49]:

$$\dot{R}^p_{\mathrm{VT}} = \rho \frac{e_{\mathrm{vib}}}{\tau_{\mathrm{VT}}} \text{ with } \frac{1}{\tau_{\mathrm{VT}}} = \sum_{\mathrm{M}} \frac{1}{\tau^{\mathrm{M}}_{\mathrm{VT}}} \,, \tag{9}$$

where τ_{VT} is a relaxation time computed from $\tau^{\mathrm{M}}_{\mathrm{VT}}$ using coefficients from Refs [50, 51] for the processes given by Eq. (R7).

The discharge power distribution $\dot{E}^p(x, y, z, t)$ follows a spatial density function $\mathcal{F}_v(x, y, z)$ and is assumed to be temporally constant during the discharge duration T_p:

$$\dot{E}^p(x, y, z, t) = \begin{cases} \frac{E^p}{T_p} \mathcal{F}_v(x, y, z) & \text{if } t' \in [0, T_p] \\ 0 & \text{otherwise} \end{cases} \text{ with } \int_V \mathcal{F}_v dV = 1 \,, \tag{10}$$

where $t' = t \bmod (1/\mathrm{PRF})$ is defined as the time from the beginning of the current pulse. The discharge duration T_p includes the high voltage pulse during which the discharge energy is deposited, and the relaxation of the electronic states. It is set to 50 ns as in Refs [21, 25, 9, 23, 24]. The spatial distribution of the plasma power $\mathcal{F}_v(x, y, z)$ is estimated as a cylinder with a radius of 500 μm and a length of 5 mm in the y-direction between the pin-to-pin electrodes. The shape and size of the discharge are obtained from plasma channel imaging (Section 2).

The numerical domain is discretized with an unstructured mesh comprised of 146 million tetrahedral elements (Fig. 6). The size of the cells is adapted according to the regions of interest. Refinement zones are applied in the dilution air mixer and after the fuel injection nozzle. Special attention is given to the discharge area where the mesh size is 120 μm. In addition, the region between the electrodes and the combustion chamber is discretized with a mesh size of 180 μm to properly capture the effects of NRPDs [9]. The combustion chamber is meshed with a cell size of 380 μm, resulting in a flame thickening factor $\mathcal{F} \approx 5$. Walls are handled with a law-of-the-wall formulation [52]. They are modeled as isothermal with a temperature of 900 and 700 K for the quartz and water-cooled aluminium parts, respectively. The quartz parts are the side walls of the sequential burner and the combustion chamber, designed for optical access. Navier–Stokes characteristic boundary conditions [53] are used for the inlets and the outlet of the domain.
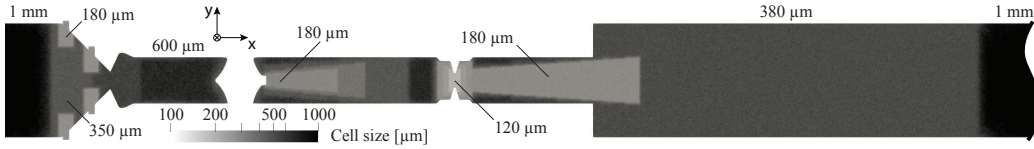
15

Figure 6: Planar cut of the mesh colored by the cell size.

4. Results and discussion

4.1. Characterization of the discharges

Detailed kinetic simulations are performed in 0D isochoric reactors using the plasma-combustion chemical mechanism developed in Ref. [20] to characterize the discharge effects. The mechanism has been extensively validated against experimental measurements of NEP discharges in air and methane-air mixtures. The measurements include: atomic oxygen production [54, 55], fast gas heating [54, 56], vibrationally excited nitrogen population [56], and ignition delay time [57]. The mechanism has been later extended to mixtures containing combustion products in Ref. [58]. Cantera [39] is coupled with the Electron Energy Distribution Function (EEDF) solver BOLOS [59] to perform 0D simulations including the detailed plasma-combustion kinetics [20]. The volume of the discharge is experimentally estimated as a cylinder with a radius of 500 μm and a length of 5 mm (Section 2). The energy density $e^p = E^p/V_d$, where V_d is the discharge volume, is $e^p = 0.308$ J/cm^3 for $E^p = 1.21$ mJ, and $e^p = 0.527$ J/cm^3 for $E^p = 2.07$ mJ.

In order to determine an initial state for the discharge, a first LES is performed on the OP "NRPD off" (Table 1). The thermochemical state variables inside the discharge volume are then spatially and temporally averaged (Table 3). From this thermochemical state, a high voltage pulse is applied until the deposited energy reaches the deposited energy measured in the experiments. The reduced electric field is estimated as $E/N = U/d/N \approx 246$ Td, where $U = 14$ kV is the applied voltage, $d = 8$ mm is the interelectrode gap distance and $N = 7.12 \times 10^{24}$ m^{-3} is the gas number density. Then, the simulation is continued up to 100 ns in order to relax the electronic excitation energy into other energy channels. Figure 7 shows the distribution of the discharge energy for the $E^p = 1.21$ mJ ($e^p = 0.308$ J/cm^3) case. The ionization energy quickly vanishes after the high voltage pulse. The electronic excitation energy relaxes during the 100 ns to reach a negligible residue as in Ref [25]. At time $t = 100$ ns, the energy fractions α_{chem}, α_{heat} and α_{vib} are

16

47.5 %, 39.9 % and 12.6 %, respectively. The α coefficients for the plasma modeling are detailed in Table 4. The specific chemical $\alpha_{i=1,...,J}$ for the J processes detailed in Table 2 are determined using the averaged molar production rates from the detailed plasma kinetic simulation [25]. Similar energy distribution is observed for $E^p = 2.07$ mJ since energy branching is governed by E/N.

T [K]	1030.6		
X_{O_2}	0.116	X_{H_2}	0.045
X_{N_2}	0.689	X_{CO_2}	0.033
X_{CH_4}	0.049	X_{H_2O}	0.068

Table 3: Thermochemical state averaged in space and time in the discharge volume. Extract from the LES computation "NRPD off". Only the species with a molar fraction $X_k \geq 10^{-3}$ are reported.
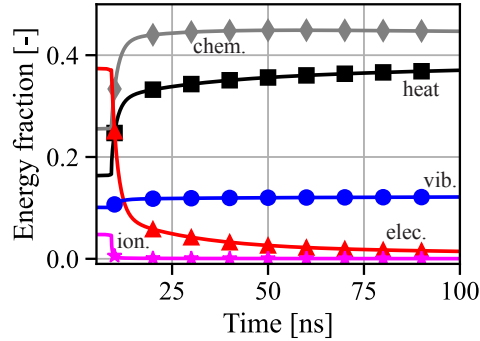
Figure 7: Distribution of the discharge energy with $E/N = 246$ Td, $e^p = 0.308$ J/cm^3, and the initial conditions given in Table 3.

α_{chem}	0.475	α_3	0.005
α_{heat}	0.399	α_4	0.076
α_{vib}	0.126	α_5	0.026
α_1	0.183	α_6	0.134
α_2	0.049	α_7	0.000

Table 4: α coefficients for the phenomenological plasma model computed from a detailed kinetic plasma simulation with $E/N = 246$ Td, $e^p = 0.308$ J/cm^3, and the initial conditions given in Table 3.

17

O, H and OH are the main species quickly produced by the discharge as shown in Fig. 8. NO is not abruptly produced during the first 10 ns. It is produced later in time due to chemical reactions that will be detailed in Section 4.3. The results of the detailed kinetics are compared with those from the phenomenological model in a similar isochoric 0D reactor (Fig. 9) using Cantera [39], where the source terms from the plasma model are simply added to the Right-Hand Side (RHS) of the governing equations. The modeling of the plasma effects does not consider the different phases of the plasma observed during the high voltage pulse and the afterglow. Thus, differences in species concentration are observed up to $t = T_p = 50$ ns. Afterwards, the evolution of the species and the ignition of the reactive mixture are very well retrieved. This validates the approach used in this work to model the effects of the NEP.
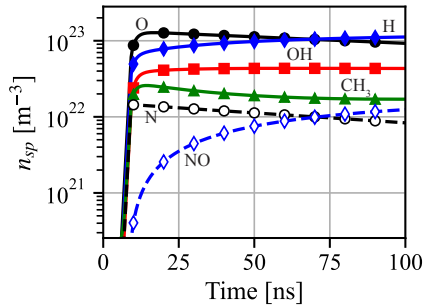
Figure 8: Number density of the main species produced by the NEP discharge with $E/N = 246$ Td, $e^p = 0.308$ J/cm^3, and the initial conditions given in Table 3.

4.2. Flame response to NRPDs

The effect of the NRPDs on the average flame position is quantified by the position of the flame Center of Gravity (COG) as depicted in Fig. 10. The flame COG is estimated using the Line-of-Sight (LOS) integration of the HRR for the LESs and the OH* chemiluminescence—used as a tracer of HRR [60]—for the experiments. The distance from the COG to the Sequential Burner (SB) outlet in the z-direction is defined as

$$Z_{\text{COG}} = \frac{\sum I_i \, (z_i - z_{\text{SB}})}{\sum I_i} \,, \tag{11}$$

where I_i is the HRR or OH* chemiluminescence intensity of the ith data point, and z_i its z-coordinate. The LES data found in the non-visible parts
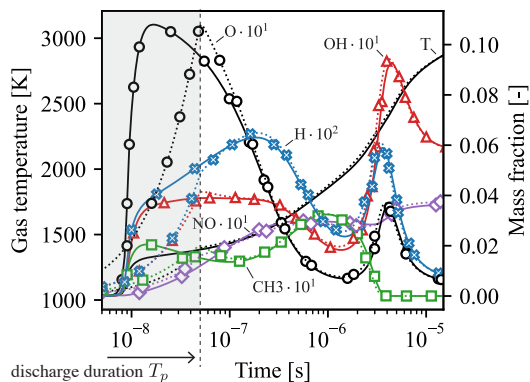
18

Figure 9: Gas temperature and species mass fraction after a NEP discharge using detailed plasma chemistry (——) and the plasma modeling approach (······). $E/N = 246$ Td, $e^p = 0.308$ J/cm^3, initial conditions given in Table 3.

of the experiments (hatched boxes in Fig. 10) are not taken into account so as not to bias the comparison. The moving back of the flame center of gravity following the application of the NRPDs is well retrieved by the LES. The absolute value of Z_{COG} differs by a few millimetres. This may be due to the experimental configuration which produces an asymmetrical flame, particularly noticeable for "NRPD off" in Fig. 10. The asymmetry is due to the design of the injector, which does not produce a perfect distribution of the fuel within the SB. Moreover, it is important to bear in mind that in non-perfectly premixed flames, the flame HRR and chemiluminescence are not directly proportional and the later is only an approximate marker of the former, the reliability of the approximation degrading with the degree of non-premixedness. Experimental images also show weak ("14kV, 20kHz") and intense ("14kV, 40kHz") chemical activity in the SB before the combustion chamber. This is also retrieved by the LES. The capability of the LES setup to capture the extension of the lean blow-off limit by NRPDs has already been demonstrated by the authors [9]. Here, it is shown that the numerical approach also reproduces the effect of plasma on the flame position. This reinforces the conclusions in Ref. [9] regarding the capability of the LES strategy to retrieve the effects of the plasma on complex combustor configurations.
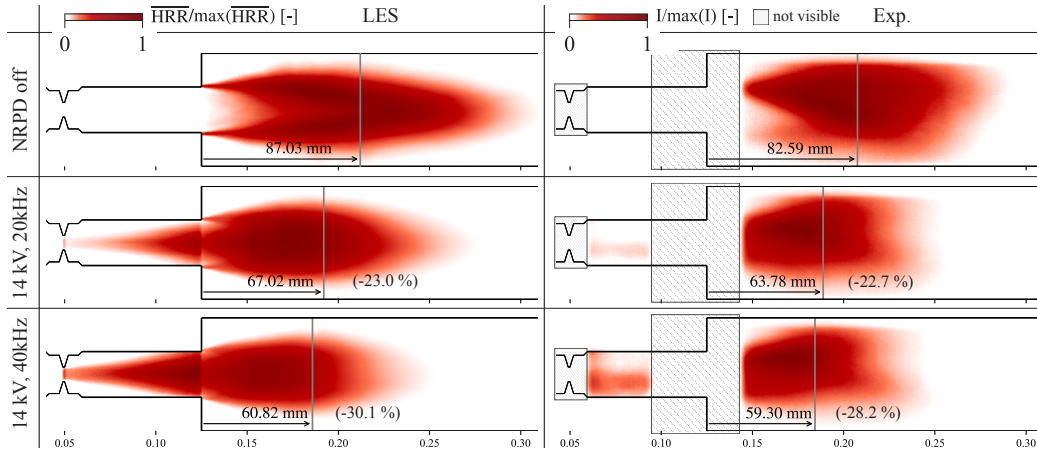
19

Figure 10: LOS integration of the average HRR from the LESs (left) and of the average OH[*] chemiluminescence from the experiments (right) at three different plasma parameters. All values are normalized with respect to their maximum value. The flame center of gravity Z_{COG} (Eq. (11)) is indicated by a vertical gray line. Areas without visual access are indicated by hatched boxes.

4.3. Nitrogen oxides chemistry

4.3.1. 3D LES results

The NO concentration experimentally measured at the probe location indicated in Fig. 1 ("Gas analyzer probe") is compared with the one from the LES to validate the modeling. The NO concentration is extracted from the LES on a plane normal to the z axis at the position of the experimental probe. First, the thermochemical state of the mixture is averaged over this plane and over time to reproduce an experimental sample. Then, H_2O is removed from the gas composition and the mixture is cooled to 276.15 K to match the conditioning of the gas sample by the gas analyzer. The absolute values obtained using LES are in very good agreement with the experimental ones (Fig. 11). The NO increase due to the 2nd stage combustion of +10 mg/Nm^3 is perfectly retrieved ("NRPD off"). The NO increase due to plasma at "14 kV, 20 kHz" (+15.5 mg/Nm^3) is also well captured. A slight deviation is observed for "14 kV, 40 kHz" where the NO increment is +27.7 instead of +34.7 mg/Nm^3 for the experiments. Overall, the increase in NO is very well retrieved by the numerical modeling. This confirms the capability of the LES setup to reproduce the effects of the NRPDs on the NO chemistry.

Figure 12 shows the NO mass fraction in the LES domain for the different OPs. The flame front is delineated with two iso-contours of progress variable
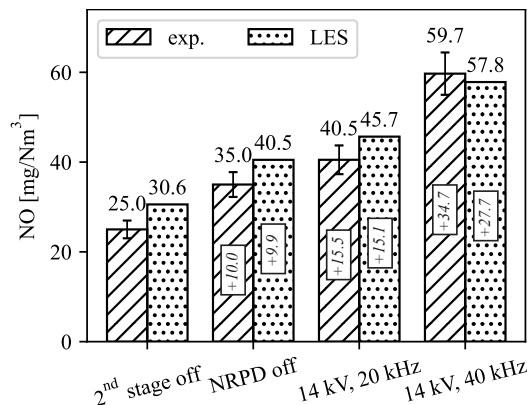
20

Figure 11: Average NO mass concentration at the probe location. Gas without H_2O and cooled to 276.15 K. The stickers show the increment compared to "2nd stage off" where the 2nd stage fuel injection and the plasma is off. Table 1 characterizes the four different OPs.

C defined as

$$C = \frac{Y_C - Y_C^u}{Y_C^b - Y_C^u} \,, \tag{12}$$

with

$$Y_C = Y_{H_2O} + Y_{CO_2} \,, \tag{13}$$

where the u and b superscripts represent the value in the unburnt and burnt gas, respectively. NO is produced right after the discharges in the kernels generated by the plasma. These kernels with high NO concentration are convected to the flame brush while distorted by and diffusing in the turbulent flow. The chemical activity within the turbulent flame in the combustion chamber does not heavily affect the NO molecules that simply flow toward the exhaust. This is also seen in Fig. 13 where NO consumption is limited within the flame fronts. However, there are zones where NO is heavily consumed after the discharge location indicated as "post-discharge destruction" in Fig. 13. They follow the intense NO production by the plasma in the discharge volume ("discharge production" in Fig. 13). In addition, zones with intense NO production are also seen after the discharge, in the SB ("post-discharge production" in Fig. 13).
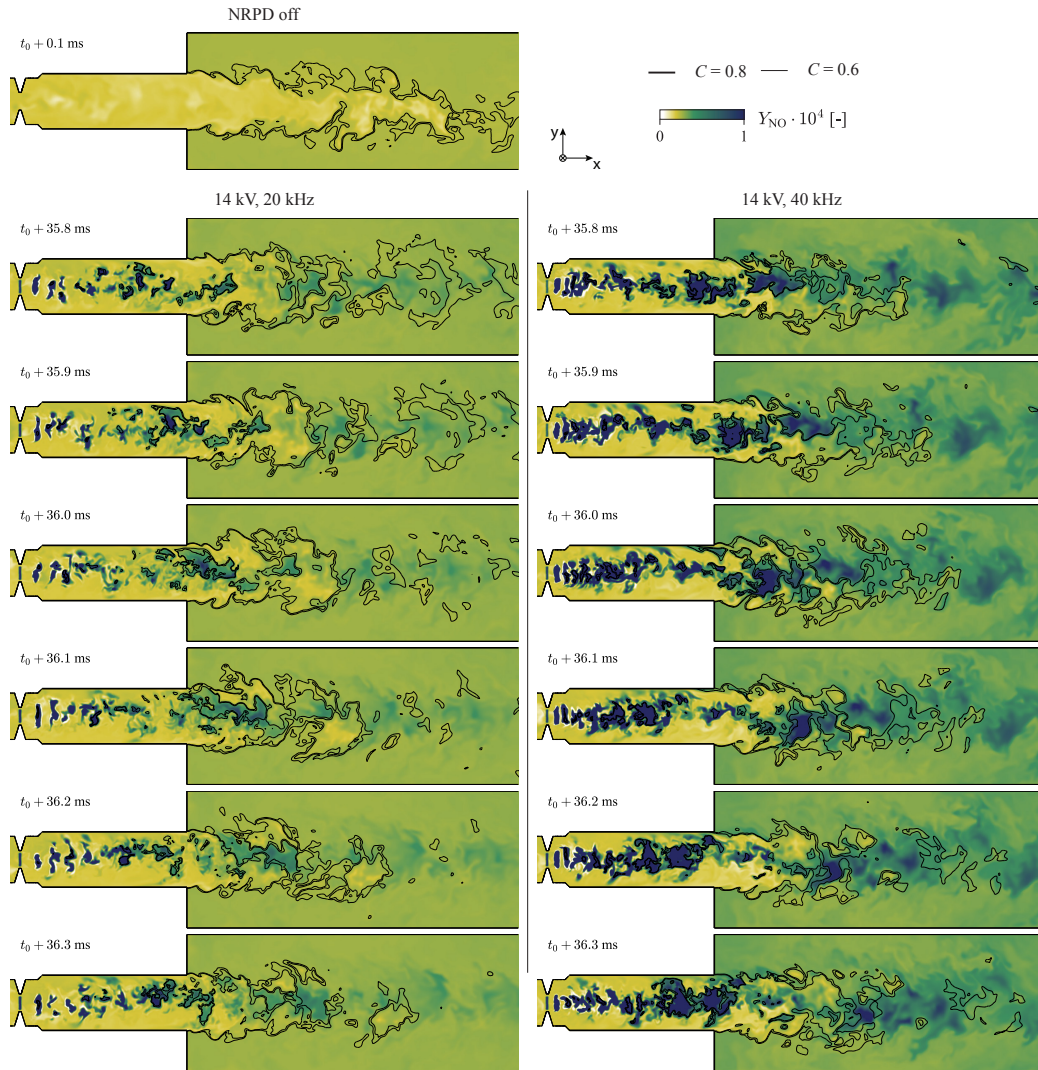
Figure 12: Planar cuts colored by the NO mass fraction with two iso-contours of progress variable C (Eq. (12)) for three different OPs.
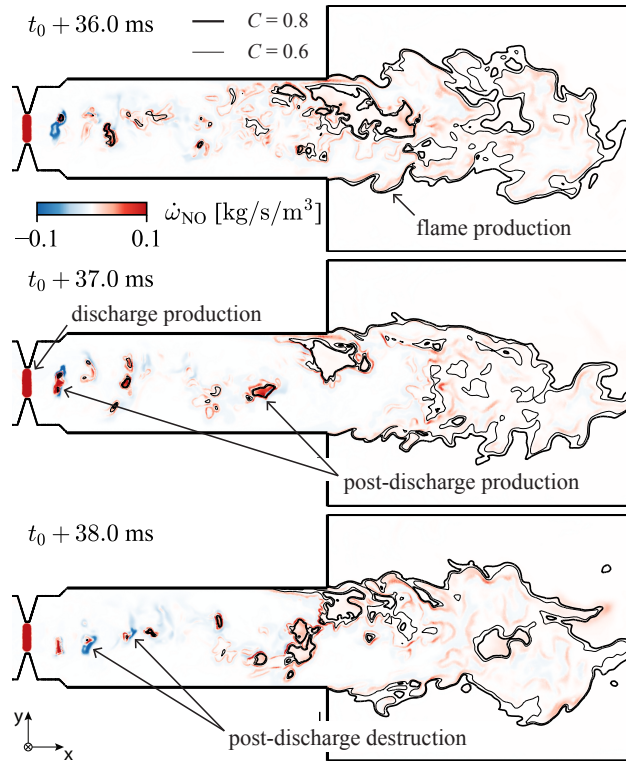
Figure 13: Planar cuts colored by the NO chemical source term with two iso-contours of progress variable C (Eq. (12)). "14 kV, 20 kHz".

4.3.2. Zero-dimensional study of the detailed chemistry

An analysis of the plasma-combustion chemistry is required to understand the kinetic pathways leading to the NO production and destruction zones. Due to the complexity of the kinetics, a 0D approach is used where the plasma reactor described in Section 4.1 is run for a longer time. For the sake of brevity, only the OP "14 kV, 20 kHz" is analyzed. The dominant reactions are the same for "14 kV, 40 kHz". Three different phases for NO production/destruction are highlighted by the molar NO source term Ω_{NO} in Fig. 14:

(1) High NO production due to the plasma discharge. The effects of the plasma (e.g., gas heating, radical production) generate NO intensively for a short period of time. The production of NO during this phase is 30.6×10^{-3} mol/m^3.

23

(2) Post-discharge NO destruction. Later in time, NO is actually consumed while combustion is occurring. The consumption of NO during this phase is 1.1×10^{-3} mol/m^3.

(3) Post-discharge NO production. During the combustion after $C \approx 0.5$, NO production rises again before fading at the end of the combustion process. The production of NO during this phase is 7.5×10^{-3} mol/m^3. This is four times less than the NO production during (1).
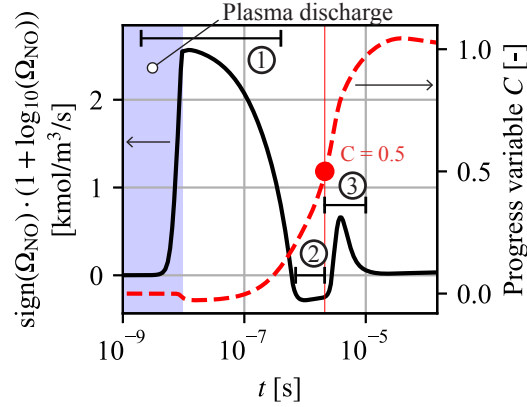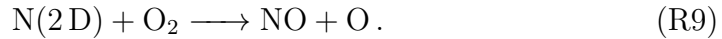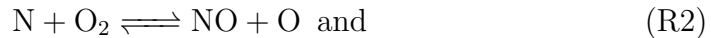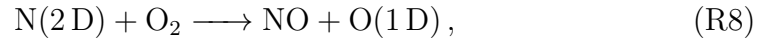

Figure 14: Magnitude of the NO molar source term Ω_{NO} after a NEP discharge using detailed plasma chemistry in a 0D plasma reactor with $E/N = 246$ Td, $e^p = 0.308$ J/cm^3, initial conditions given in Table 3. The blue area represent the discharge period during which the electric field is applied. The progress variable C (Eq. (12)) shows the combustion advancement. (1) NO plasma production, (2) NO consumption, (3) post-discharge NO production.

The NO production rates due to the specific chemical reactions in these three phases are shown in Fig. 15. Plasma NO production in phase (1) is mainly due to the presence of atomic N and N(2D), which react with O$_2$ and OH to form NO molecules via the reactions:

$$\mathrm{N(2\,D) + O_2 \longrightarrow NO + O(1\,D)}, \tag{R8}$$

$$\mathrm{N + OH \rightleftharpoons H + NO}, \tag{R3}$$

$$\mathrm{N + O_2 \rightleftharpoons NO + O} \text{ and} \tag{R2}$$

$$\mathrm{N(2\,D) + O_2 \longrightarrow NO + O}. \tag{R9}$$

24

For this case, N and N(2D) are mainly produced by the electron impact reaction

$$e^- + N_2 \longrightarrow e^- + N + N(2\,D)\,. \tag{R10}$$
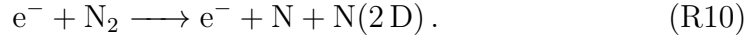
One might have expected the reaction

$$N_2 + O \rightleftharpoons NO + N \tag{R6}$$
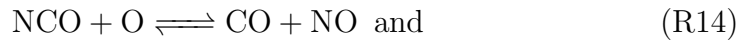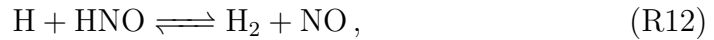
to be a source of NO production because of the atomic oxygen produced by the plasma (Fig. 8). However, the backward reaction rate dominates the forward reaction rate in Eq. (R6) during this period. Thereby, NO is effectively consumed by this reaction.

The NO consumption observed in phase (2) is mainly due to "reburn" mechanisms where NO reacts with hydrocarbons and is subsequently reduced via

$$CH_i + NO \longrightarrow products\,, \tag{R11}$$
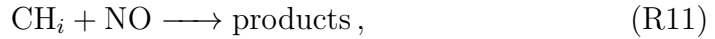
with i $= 1, 2, 3$. This logically coincides with the start of the combustion, when CH_4 is decomposed via the oxidation process.

After the fuel oxidation phase during the combustion process (phase (3)), N atoms still play a role via the Eqs (R2) and (R3). In addition, reactions part of the so-called "prompt" mechanism [61] play a role in the NO production. They are mainly:

$$H + HNO \rightleftharpoons H_2 + NO\,, \tag{R12}$$

$$NH + O \rightleftharpoons H + NO\,, \tag{R13}$$

$$NCO + O \rightleftharpoons CO + NO \text{ and} \tag{R14}$$

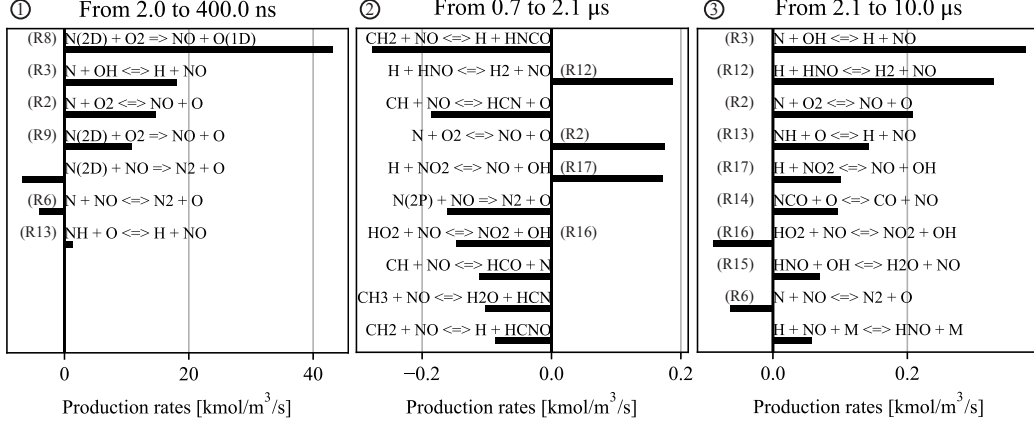$$HNO + OH \rightleftharpoons H_2O + NO\,. \tag{R15}$$

Figure 15: Averaged NO production rates for the three different periods annotated in Fig. 14. Only the highest fluxes are shown. $E/N = 246$ Td, $e^p = 0.308$ J/cm^3, initial conditions given in Table 3.

4.3.3. Study of the LES chemistry

The NO chemistry is now studied in the complex 3D turbulent environment of the sequential burner from the LES for the OP "14 kV, 20 kHz". In order to identify the reactions responsible for NO production and consumption, an index of production $I_{\mathrm{NO}}^{P,j}$ and of consumption $I_{\mathrm{NO}}^{C,j}$ are defined for every reaction j. They read

$$I_{\mathrm{NO}}^{P,j} = \frac{\nu_{\mathrm{NO}}^{j} Q^{j}}{\Omega_{\mathrm{NO}}^{P}} \text{ and} \tag{14}$$

$$I_{\mathrm{NO}}^{C,j} = \frac{\nu_{\mathrm{NO}}^{j} Q^{j}}{\Omega_{\mathrm{NO}}^{C}} \,, \tag{15}$$

where ν_{NO}^{j} and Q^{j} are the stoichiometric coefficient of NO and the rate of progress of the reaction j, respectively. Ω_{NO}^{P} and Ω_{NO}^{C} represent the production and consumption rate of NO and are defined as

$$\Omega_{\mathrm{NO}}^{P} = \sum_{j} \max\left(\nu_{\mathrm{NO}}^{j} Q^{j}, 0\right) \text{ and} \tag{16}$$

$$\Omega_{\mathrm{NO}}^{C} = \sum_{j} \min\left(\nu_{\mathrm{NO}}^{j} Q^{j}, 0\right) \,. \tag{17}$$

Figure 16 shows the most important NO production indexes on a plane through the Sequential Burner (SB) at the end of the occurrence of a NEP

26

discharge. The plasma global process no. 3 (Table 2) is the main source of NO in the discharge zone. The reactions (R2) and (R3) play a secondary role in this region. The species generated by the plasma (Table 2) provide a favorable environment for the development of these two reactions. Reactions (R12) and (R13) from the prompt NO mechanism play a role later in the igniting kernels as in Fig. 15. A conversion of NO_2, another component of nitrogen oxides, to NO is also observed both in the plasma-induced igniting kernels and in the main flame brush.
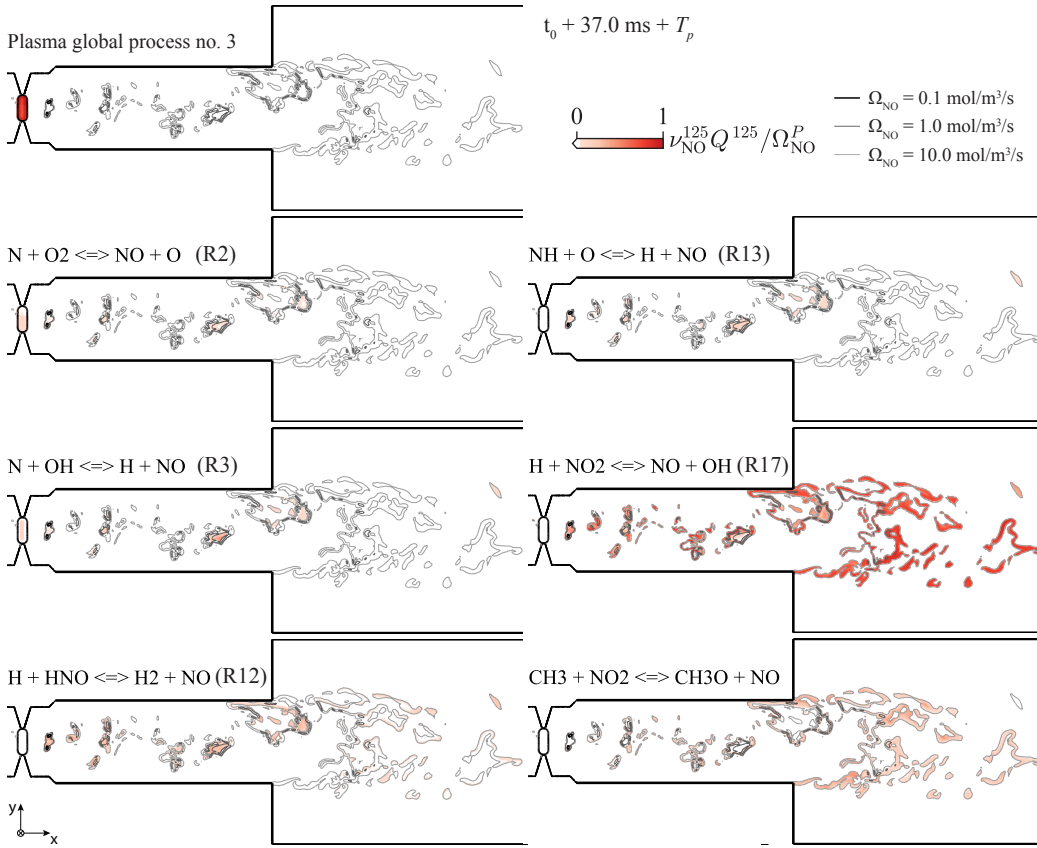

Figure 16: Planar cuts colored by the NO production index (Eq. (14)) with three iso-contours of NO molar source term Ω_{NO}. "14 kV, 20 kHz". Snapshot at the end of the occurrence of a NEP discharge.

The destruction/consumption of NO in the SB after the discharge location is mainly due to a single reaction (Fig. 17):

$$HO_2 + NO \rightleftharpoons NO_2 + OH. \tag{R16}$$

27

This reaction takes place next to the NO production zones, on the fresh gas side. This is due to the diffusion of NO molecules into the fresh gas containing HO_2 radicals. Hydroperoxyl is strongly present in the hot mixture of vitiated air and fuel that flows through the SB and undergoes the first stages of the auto-ignition process. This cannot be retrieved by the 0D study performed in Section 4.3.2 because no exchange with the surrounding environment is considered. Reburn processes (Eq. (R11)) do not effectively participate in NO depletion in the turbulent flow. This is due to the low magnitude of the associated source term shown in Fig. 14, phase (2).
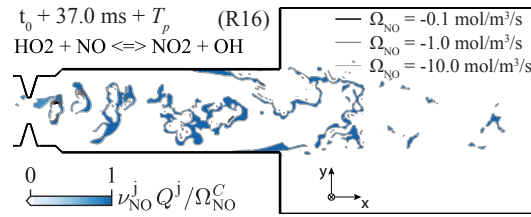

Figure 17: Planar cut colored by the NO consumption index (Eq. (15)) with three iso-contours of NO molar source term Ω_{NO}. "14 kV, 20 kHz". Snapshot at the end of the occurrence of a NEP discharge.

4.3.4. Impact of the nitrogen plasma chemistry

To evaluate the impact of the nitrogen plasma chemistry on the NO production the coefficient α_2 and α_3 are set to zero. These coefficients are responsible for the production of N and NO in the phenomenological plasma model employed (Table 2). Figure 18 shows the mass fraction of NO significantly lower than the one obtained taking into account the nitrogen plasma chemistry (Fig. 12). To limit the computational time, the concentration is extracted 250 mm after the inlet of the 2nd stage combustion chamber, rather than 450 mm where the experimental probe is located. This is possible here because no comparison with experimental data is made and the LES setup has already been validated in Sections 4.2 and 4.3.1. The NO concentration (gas without H_2O and cooled to 276.15 K) increases only slightly when $\alpha_2 = \alpha_3 = 0$ (+0.4 mg/Nm^3 and +2.5 mg/Nm^3 for "14 kV, 20 kHz" and "14 kV, 40 kHz", respectively), whereas it increases significantly when plasma nitrogen chemistry is considered (+6.0 mg/Nm^3 and +16.7 mg/Nm^3 for "14 kV, 20 kHz" and "14 kV, 40 kHz", respectively) compared to the case without NRPD. This demonstrates the importance of taking into ac-

28

count nitrogen plasma chemistry for the correct prediction of NO emissions during plasma assisted combustion.
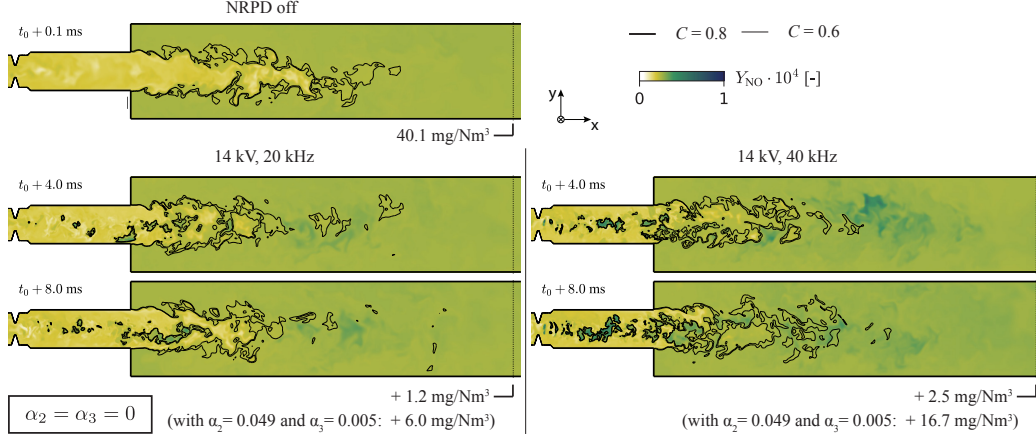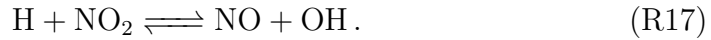

Figure 18: Planar cuts colored by the NO mass fraction with two iso-contours of progress variable C (Eq. (12)). The nitrogen chemistry is removed from the plasma modeling (i.e., $\alpha_2 = \alpha_3 = 0$ in Table 4). The NO concentration is extracted from a plane normal to the z axis, delineated by a dotted line, 250 mm after the inlet of the 2nd stage combustion chamber.

The NO production index (Eq. (14)) of the most important reactions for NO production is shown in Fig. 19. Since the production of atomic N by the plasma is disabled, the reactions (R2) and (R3) no longer take place in the discharge zone. They are delayed and are now taking place in the igniting kernels together with the initiation reaction of the thermal NO pathway defined by Zel'dovich

$$N_2 + O \rightleftharpoons NO + N. \tag{R6}$$

The generation of NO due to the plasma-generated species in the discharge zone is now mainly due to the presence of H atoms induced by the processes 4 and 6 in Table 2. NO_2 from the 1st stage combustion reacts with H to produce NO via

$$H + NO_2 \rightleftharpoons NO + OH. \tag{R17}$$

Prompt mechanism still plays a role with the reactions (R12), (R13) and

$$NCN + O \rightleftharpoons CN + NO. \tag{R18}$$
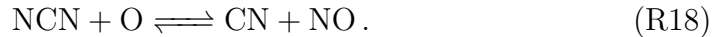
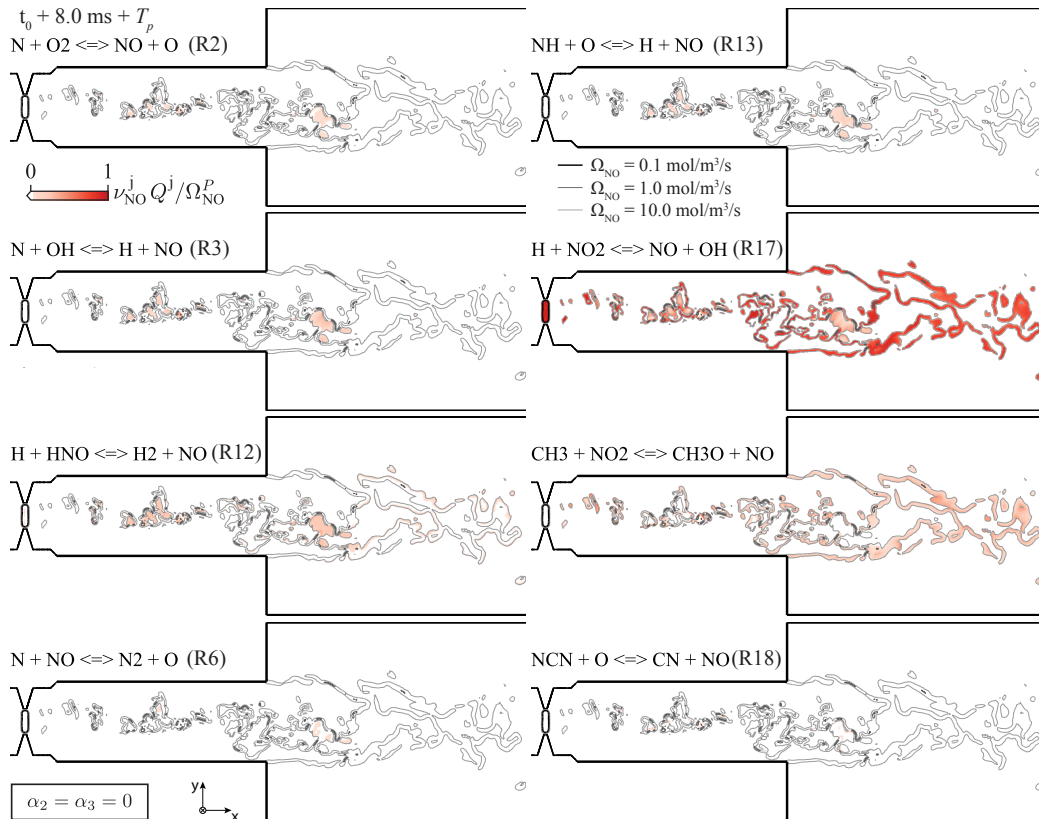Similar results are found for "14 kV, 40 kHz".

Figure 19: Planar cuts colored by the NO production index (Eq. (14)) with three iso-contours of NO molar source term Ω_{NO}. "14 kV, 20 kHz". The nitrogen chemistry is removed from the plasma modeling (i.e., $\alpha_2 = \alpha_3 = 0$ in Table 4). Snapshot at the end of the occurrence of a NEP discharge.

5. Conclusion

The formation of NO during plasma assisted combustion in a lab-scale sequential combustor was investigated using numerical simulation tools. The complex 3D turbulent reactive flow has been simulated with a LES approach, including a precise description of the chemical kinetics and an accurate modeling of the plasma effects. Simulation results were found to be in very good agreement with experimental measurements, including OH^* chemiluminescence imaging and NO sampling at the burner outlet. The 3D analysis is complemented by detailed 0D plasma computations.

For the operating points studied, the NO formation is mainly due to the dissociation of N_2 by direct electron impact. This generates nitrogen atoms that react with OH and O_2 to form NO in the sequential burner. Within the flame brush, the prompt mechanism slightly participates to the NO formation, without drastically changing the concentration. Removing the modeling of the nitrogen plasma chemistry from the description of the plasma effects leads to a strong underestimation of the NO formation. This shows the limited participation of the thermal routes in the formation of NO. In addition, this demonstrates the need for an advanced modeling approach of the NEP in order to study the formation of undesirable species such as NO.

More generally, this study is the first to identify the NO formation pathways when NRPDs are applied in a turbulent-flow combustor. The excellent agreement with experiments demonstrates the capability of the LES setup to retrieve NRPD effects on combustion and NO formation. This work demonstrates how leading-edge simulation tools can help research on innovative combustion technology.

To optimize the application of NRPDs to combustion systems, particular attention needs to be paid to the reactions causing N_2 dissociation, found to be mainly responsible for the formation of NO. Work is underway to identify the NRPD key parameters that trigger the dissociation of nitrogen molecules, in order to give design indications for practical applications. It is possible that the contribution of kinetic pathways to NO_x formation will change for other OPs, especially at higher equivalence ratio or operating pressure. Experiments at higher pressures are currently in progress in our laboratory to investigate this open question.

Acknowledgement

References

[1] Y. Ju, W. Sun, Plasma assisted combustion: Progress, challenges, and opportunities, Combust. Flame 162 (3) (2015) 529–532.

[2] D. A. Lacoste, Flames with plasmas, Proc. Combust. Inst. 39 (4) (2022) 5405–5428.

[3] G. L. Pilla, D. A. Lacoste, D. Veynante, C. O. Laux, Stabilization of a Swirled Propane–Air Flame Using a Nanosecond Repetitively Pulsed Plasma, IEEE Trans. Plasma Sci. 36 (4) (2008) 940–941.

[4] S. Barbosa, G. Pilla, D. A. Lacoste, P. Scouflaire, S. Ducruix, C. O. Laux, D. Veynante, Influence of nanosecond repetitively pulsed discharges on the stability of a swirled propane/air burner representative of an aeronautical combustor, Philos. Trans. R. Soc. A Math. Phys. Eng. Sci. 373 (2048) (2015).

[5] Y. Xiong, O. Schulz, C. Bourquard, M. Weilenmann, N. Noiray, Plasma enhanced auto-ignition in a sequential combustor, Proc. Combust. Inst. 37 (4) (2019) 5587–5594.

[6] F. Di Sabatino, D. A. Lacoste, Enhancement of the lean stability and blow-off limits of methane-air swirl flames at elevated pressures by nanosecond repetitively pulsed discharges, J. Phys. D. Appl. Phys. 53 (35) (2020).

[7] G. Vignat, N. Minesi, P. R. Soundararajan, D. Durox, A. Renaud, V. Blanchard, C. O. Laux, S. Candel, Improvement of lean blow out performance of spray and premixed swirled flames using nanosecond

repetitively pulsed discharges, Proc. Combust. Inst. 38 (4) (2021) 6559–6566.

[8] S. A. Shcherbanev, Q. Malé, B. Dharmaputra, R. Solana-Pérez, N. Noiray, Effect of plasma-flow coupling on the ignition enhancement with non-equilibrium plasma in a sequential combustor, J. Phys. D. Appl. Phys. 55 (42) (2022).

[9] Q. Malé, S. Shcherbanev, N. Noiray, Numerical study of plasma assisted combustion in a sequential combustor, Proc. Combust. Inst. 39 (4) (2022) 5447–5456.

[10] D. A. Lacoste, J. P. Moeck, D. Durox, C. O. Laux, T. Schuller, Effect of nanosecond repetitively pulsed discharges on the dynamics of a swirl-stabilized lean premixed flame, J. Eng. Gas Turbines Power 135 (10) (2013).

[11] J. P. Moeck, D. A. Lacoste, C. O. Laux, C. O. Paschereit, Control of combustion dynamics in a swirl-stabilized combustor with nanosecond repetitively pulsed discharges, in: 51st AIAA Aerosp. Sci. Meet. Incl. New Horizons Forum Aerosp. Expo. 2013, 2013.

[12] S. Shcherbanev, T. Morinière, R. Solana-Pérez, M. Weilenmann, Y. Xiong, U. Doll, N. Noiray, Anchoring of premixed jet flames in vitiated crossflow with pulsed nanosecond spark discharge, Appl. Energy Combust. Sci. (2020).

[13] F. DI Sabatino, T. F. Guiberti, J. P. Moeck, W. L. Roberts, D. A. Lacoste, Actuation efficiency of nanosecond repetitively pulsed discharges for plasma-assisted swirl flames at pressures up to 3 bar, J. Phys. D. Appl. Phys. 54 (7) (2021).

[14] W. Kim, H. Do, M. G. Mungal, M. A. Cappelli, Investigation of NO production and flame structure in plasma enhanced premixed combustion, Proc. Combust. Inst. 31 II (2007) 3319–3326.

[15] D. A. Lacoste, J. P. Moeck, C. O. Paschereit, C. O. Laux, Effect of plasma discharges on nitric oxide emissions in a premixed flame, J. Propuls. Power 29 (3) (2013) 748–751.

[16] G. T. Kim, B. H. Seo, W. J. Lee, J. Park, M. K. Kim, S. M. Lee, Effects of applying non-thermal plasma on combustion stability and emissions of NOx and CO in a model gas turbine combustor, Fuel 194 (2017) 321–328.

[17] N. A. Popov, Investigation of the mechanism for rapid heating of nitrogen and air in gas discharges, Plasma Phys. Reports 27 (10) (2001) 886–896.

[18] A. Bellemans, N. Kincaid, N. Deak, P. Pepiot, F. Bisetti, P-DrGEP: A novel methodology for the reduction of kinetics mechanisms for plasma-assisted combustion applications, Proc. Combust. Inst. 38 (4) (2021) 6631–6639.

[19] A. Bellemans, N. Deak, F. Bisetti, Development of skeletal kinetics mechanisms for plasma-assisted combustion via principal component analysis, Plasma Sources Sci. Technol. 29 (2) (2020).

[20] L. Cheng, N. Barleon, B. Cuenot, O. Vermorel, A. Bourdon, Plasma assisted combustion of methane-air mixtures: Validation and reduction, Combust. Flame 240 (2022).

[21] M. Castela, B. Fiorina, A. Coussement, O. Gicquel, N. Darabiha, C. O. Laux, Modelling the impact of non-equilibrium discharges on reactive mixtures for simulations of plasma-assisted ignition in turbulent flows, Combust. Flame 166 (2016) 133–147.

[22] M. Castela, S. Stepanyan, B. Fiorina, A. Coussement, O. Gicquel, N. Darabiha, C. O. Laux, A 3-D DNS and experimental study of the effect of the recirculating flow pattern inside a reactive kernel produced by nanosecond plasma discharges in a methane-air mixture, Proc. Combust. Inst. 36 (3) (2017) 4095–4103.

[23] Y. Bechane, B. Fiorina, Numerical investigations of turbulent premixed flame ignition by a series of Nanosecond Repetitively Pulsed discharges, Proc. Combust. Inst. 38 (4) (2021) 6575–6582.

[24] Y. Bechane, B. Fiorina, Numerical analysis of turbulent flame enhancement by nanosecond repetitively pulsed plasma discharges, Proc. Combust. Inst. 39 (4) (2022) 5465–5476.

[25] N. Barléon, L. Cheng, B. Cuenot, O. Vermorel, A phenomenological model for plasma-assisted combustion with NRP discharges in methane-air mixtures: PACMIND, Combust. Flame 253 (2023).

[26] A. Felden, Development of Analytically Reduced Chemistries (ARC) and applications in Large Eddy Simulations (LES) of turbulent combustion., Ph.D. thesis, Université de Toulouse (2017).

[27] T. Jaravel, E. Riber, B. Cuenot, G. Bulat, Large Eddy Simulation of an industrial gas turbine combustor using reduced chemistry with accurate pollutant prediction, Proc. Combust. Inst. 36 (3) (2017) 3817–3825.

[28] B. Rochette, F. Collin-Bastiani, L. Gicquel, O. Vermorel, D. Veynante, T. Poinsot, Influence of chemical schemes, numerical method and dynamic turbulent combustion modeling on LES of premixed turbulent flames, Combust. Flame 191 (2018) 417–430.

[29] Q. Malé, O. Vermorel, F. Ravet, T. Poinsot, Direct numerical simulations and models for hot burnt gases jet ignition, Combust. Flame 223 (2021) 407–422.

[30] T. Capurso, D. Laera, E. Riber, B. Cuenot, NOx pathways in lean partially premixed swirling H2-air turbulent flame, Combust. Flame 248 (2023).

[31] Q. Cazères, P. Pepiot, E. Riber, B. Cuenot, A fully automatic procedure for the analytical reduction of chemical kinetics mechanisms for Computational Fluid Dynamics applications, Fuel 303 (2021).

[32] P. Pepiot-Desjardins, H. Pitsch, An efficient error-propagation-based reduction method for large chemical kinetic mechanisms, Combust. Flame 154 (1-2) (2008) 67–81.

[33] P. Pepiot-Desjardins, H. Pitsch, An automatic chemical lumping method for the reduction of large chemical kinetic mechanisms, Combust. Theory Model. 12 (6) (2008) 1089–1108.

[34] T. Løvås, F. Mauss, C. Hasse, N. Peters, Development of adaptive kinetics for application in combustion systems, Proc. Combust. Inst. 29 (1) (2002) 1403–1410.

[35] E. Ranzi, A. Frassoldati, A. Stagni, M. Pelucchi, A. Cuoci, T. Faravelli, Reduced kinetic schemes of complex reaction systems: Fossil and biomass-derived transportation fuels, Int. J. Chem. Kinet. 46 (9) (2014) 512–542.

[36] G. Bagheri, E. Ranzi, M. Pelucchi, A. Parente, A. Frassoldati, T. Faravelli, Comprehensive kinetic study of combustion technologies for low environmental impact: MILD and OXY-fuel combustion of methane, Combust. Flame 212 (2020) 142–155.

[37] Y. Song, L. Marrodán, N. Vin, O. Herbinet, E. Assaf, C. Fittschen, A. Stagni, T. Faravelli, M. U. Alzueta, F. Battin-Leclerc, The sensitizing effects of NO 2 and NO on methane low temperature oxidation in a jet stirred reactor, Proc. Combust. Inst. 37 (1) (2019) 667–675.

[38] W. Sun, M. Uddi, S. H. Won, T. Ombrello, C. Carter, Y. Ju, Kinetic effects of non-equilibrium plasma-assisted methane oxidation on diffusion flame extinction limits, Combust. Flame 159 (1) (2012) 221–229.

[39] D. G. Goodwin, H. K. Moffat, I. Schoegl, R. L. Speth, B. W. Weber, Cantera: An object-oriented software toolkit for chemical kinetics, thermodynamics, and transport processes, https://www.cantera.org, version 2.6.0 (2022).

[40] T. Schönfeld, M. Rudgyard, Steady and unsteady flow simulations using the hybrid flow solver AVBP, AIAA J. 37 (11) (1999) 1378–1385.

[41] L. Y. Gicquel, N. Gourdain, J. F. Boussuge, H. Deniau, G. Staffelbach, P. Wolf, T. Poinsot, Calcul parallèle haute performance des écoulements en géométries complexes, Comptes Rendus - Mec. 339 (2-3) (2011) 104–124.

[42] O. Colin, M. Rudgyard, Development of High-Order Taylor-Galerkin Schemes for LES, J. Comput. Phys. 162 (2) (2000) 338–371.

[43] F. Nicoud, H. B. Toda, O. Cabrit, S. Bose, J. Lee, Using singular values to build a subgrid-scale model for large eddy simulations, Phys. Fluids 23 (8) (2011).

[44] O. Colin, F. Ducros, D. Veynante, T. Poinsot, A thickened flame model for large eddy simulations of turbulent premixed combustion, Phys. Fluids 12 (7) (2000) 1843–1863.

[45] J. P. Legier, T. Poinsot, D. Veynante, Dynamically thickened flame LES model for premixed and non-premixed turbulent combustion, Proc. Summer Program, Cent. Turbul. Res. (2000) 157–168.

[46] F. Charlette, C. Meneveau, D. Veynante, A power-law flame wrinkling model for LES of premixed turbulent combustion Part I: Non-dynamic formulation and initial tests, Combust. Flame 131 (1-2) (2002) 159–180.

[47] O. Schulz, U. Doll, D. Ebi, J. Droujko, C. Bourquard, N. Noiray, Thermoacoustic instability in a sequential combustor: Large eddy simulation and experiments, Proc. Combust. Inst. 37 (4) (2019) 5325–5332.

[48] L. Landau, E. Teller, Zur theorie der schalldispersion, Phys. Z. Sowjet. (1936).

[49] M. Capitelli, C. Ferreira, B. Gordiets, A. Osipov, Plasma Kinetics in Atmospheric Gases, Springer Series on Atomic, Optical, and Plasma Physics, Springer Berlin Heidelberg, 2011.

[50] A. Starikovskiy, N. Aleksandrov, Plasma-assisted ignition and combustion, Prog. Energy Combust. Sci. 39 (1) (2013) 61–110.

[51] R. C. Millikan, D. R. White, Systematics of Vibrational Relaxation, The Journal of Chemical Physics 39 (12) (1963) 3209–3213.

[52] P. Schmitt, T. Poinsot, B. Schuermans, K. P. Geigle, Large-eddy simulation and experimental study of heat transfer, nitric oxide emissions and combustion instability in a swirled turbulent high-pressure burner, J. Fluid Mech. 570 (2007) 17–46.

[53] T. J. Poinsot, S. K. Lelef, Boundary conditions for direct simulations of compressible viscous flows, J. Comput. Phys. 101 (1) (1992) 104–129.

[54] D. L. Rusterholtz, D. A. Lacoste, G. D. Stancu, D. Z. Pai, C. O. Laux, Ultrafast heating and oxygen dissociation in atmospheric pressure air by nanosecond repetitively pulsed discharges, J. Phys. D. Appl. Phys. 46 (46) (2013).

[55] M. Uddi, N. Jiang, E. Mintusov, I. V. Adamovich, W. R. Lempert, Atomic oxygen measurements in air and air/fuel nanosecond pulse discharges by two photon laser induced fluorescence, Proc. Combust. Inst. 32 I (1) (2009) 929–936.

[56] A. Montello, Z. Yin, D. Burnette, I. V. Adamovich, W. R. Lempert, Picosecond CARS measurements of nitrogen vibrational loading and rotational/translational temperature in non-equilibrium discharges, J. Phys. D. Appl. Phys. 46 (46) (2013).

[57] N. L. Aleksandrov, S. V. Kindysheva, E. N. Kukaev, S. M. Starikovskaya, A. Y. Starikovskii, Simulation of the ignition of a methane-air mixture by a high-voltage nanosecond discharge, Plasma Phys. Reports 35 (10) (2009) 867–882.

[58] N. Barléon, Detailed modeling and simulations of nanosecond repetitively pulsed discharges for plasma-assisted combustion., Ph.D. thesis, Université de Toulouse (2022).

[59] G. J. Hagelaar, L. C. Pitchford, Solving the Boltzmann equation to obtain electron transport coefficients and rate coefficients for fluid models, Plasma Sources Sci. Technol. 14 (4) (2005) 722–733.

[60] J. G. Lee, D. A. Santavicca, Experimental Diagnostics for the Study of Combustion Instabilities in Lean Premixed Combustors, J. Propuls. Power 19 (5) (2003) 735–750.

[61] N. Lamoureux, P. Desgroux, A. El Bakali, J. F. Pauwels, Experimental and numerical study of the role of NCN in prompt-NO formation in low-pressure CH4-O2-N2 and C2H2-O2-N2 flames, Combust. Flame 157 (10) (2010) 1929–1941.